International Communications in Heat and Mass Transfer 155 (2024) 107558

Contents lists available at ScienceDirect

International Communications in Heat and Mass Transfer

journal homepage: www.elsevier.com/locate/ichmt

Enhanced immersion cooling using laser-induced graphene for Li-ion battery thermal management

EuiBeen Jung [a], Daeyoung Kong [b,d], Minsoo Kang [a], Juho Park [a], Jun-Hyeong Kim [c], Jinho Jeong [c], Jung Bin In [d], Ki-Yong Oh [c,**], Hyoungsoon Lee [a,d,*]

[a] Department of Intelligent Energy and Industry, Chung-Ang University, Seoul 06974, South Korea
[b] Department of Mechanical Engineering, Stanford University, Stanford, CA 94305, USA
[c] Department of Mechanical Convergence Engineering, Hanyang University, Seoul 04763, South Korea
[d] School of Mechanical Engineering, Chung-Ang University, Seoul 06974, South Korea

ARTICLE INFO

Keywords:
Battery thermal management
Immersion cooling
Boiling heat transfer
Laser-induced graphene
Electric vehicles

ABSTRACT

Efforts to mitigate environmental pollution from the use of petroleum-based energy sources have promoted research on rechargeable secondary batteries for applications such as electric vehicles and energy storage systems. In this context, Li-ion batteries have attracted significant interest. Notably, the thermal management of such batteries is crucial for achieving a stable output and long lifespan and reducing the risk of thermal runaway. Despite extensive exploration of various cooling schemes, thermal management techniques for Li-ion batteries continue to face challenges due to the high thermal resistance resulting from low thermal conductivity of thermal interfacial materials and inadequate convective heat transfer. Therefore, this study is aimed at using laser-induced graphene (LIG) to enhance the heat transfer characteristics and battery thermal management. LIG is applied through direct laser irradiation on the polyimide substrate of a $LiFePO_4$ battery. Thermal tests conducted under a discharge rate of 5C demonstrate that immersion cooling using HFE-7000 on the LIG surface substantially reduces the temperature increase by up to 84.3% compared with conventional air cooling. In addition, immersion cooling with LIG surfaces results in outstanding cooling performance through nucleate boiling, attaining a maximum temperature of 37.5 °C, which is lower than that (43.5 °C) on a pristine polyimide surface. Overall, this research provides valuable insights into the thermal management of high-performance batteries operating under extreme conditions, such as high-speed charging, high-power discharging, and high-temperature conditions, with significant implications for future applications.

1. Introduction

The mitigation of environmental pollution and greenhouse gas emissions has emerged as a matter of global concern [1]. Approximately 65% of the total emissions is attributable to the use of petroleum-based energy sources, which generates a considerable amount of harmful pollutants [2]. Thus, the development of electric vehicles (EVs) and energy storage systems (ESSs) has attracted increasing attention [3,4]. Lithium-based batteries are extensively used in ESSs and EVs because of their exceptional energy density and long lifespan [5]. Lithium-ion batteries can be classified according to the cathode materials, with notable variants including nickel-cobalt-manganese compositions in various ratios, nickel-cobalt-aluminum, and $LiFePO_4$ (LFP) and $LiMnPO_4$ batteries that use transition metal phosphates [6,7]. Among these, LFP batteries have recently garnered considerable attention as next-generation batteries owing to their high thermal and chemical stability, which render them less susceptible to thermal runaway (TR) [8,9].

Research on batteries encompasses a broad spectrum of subjects, including material analysis, capacity degradation, charge methodologies, and thermal management [10–13]. In this domain, two research hotspots are the reduced cycle life owing to battery degradation and safety concerns associated with TR phenomena [14]. Researchers have observed that high temperatures can exacerbate the deterioration of cycle life [15], with reductions of up to 65% [16]. Moreover, uneven temperature distribution can lead to localized imbalances in the state-of-

* Corresponding author at: School of Mechanical Engineering, Chung-Ang University, Seoul 06974, South Korea.
** Corresponding author at: Department of Mechanical Convergence Engineering, Hanyang University, Seoul 04763, South Korea.
E-mail addresses: kiyongoh@hanyang.ac.kr (K.-Y. Oh), leeh@cau.ac.kr (H. Lee).

https://doi.org/10.1016/j.icheatmasstransfer.2024.107558

Available online 15 May 2024

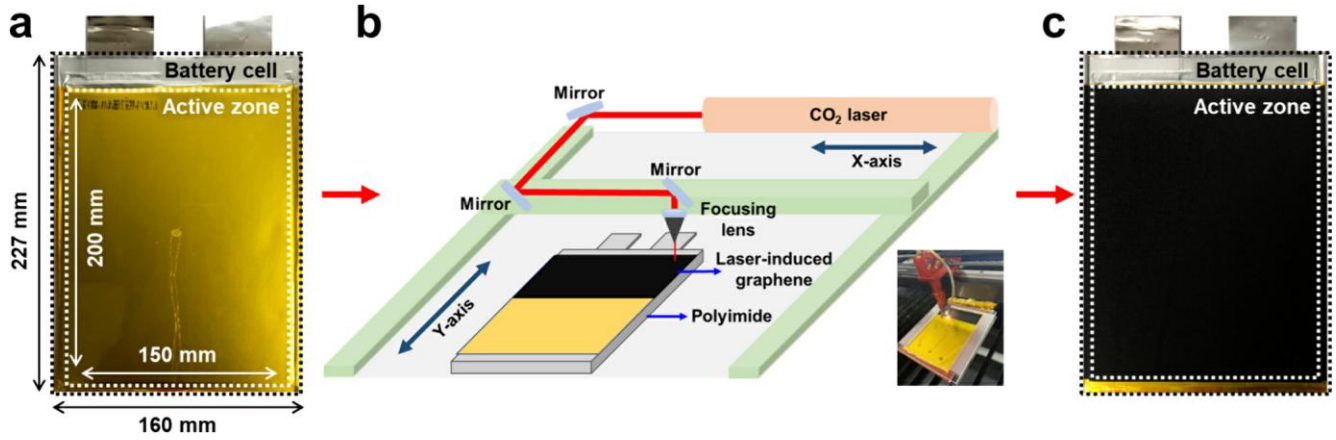

Fig. 1. Fabrication of laser-induced-graphene-coated battery. (a) Pristine polyimide coated $LiFePO_4$ battery; (b) micro-fabrication process of LIG using CO_2 laser; (c) microporous-structured LIG is produced on the $LiFePO_4$ battery with 14.5% of the maximum power, irradiation speed of 200 mm/s, and an irradiation interval of 200 μm.

charge, which further contributes to the decrease in cycle life [17–19]. Additionally, Chen et al. experimentally observed that TR can occur at a low temperature of 48.1 °C [20] and likely to occur at higher discharge rate [21], with subsequent chain reactions increasing the temperature to as high as 1000 °C [22,23]. Therefore, effective cooling methods for such batteries must be identified.

To ensure stable battery operation while alleviating cycle life degradation and potential TR risks, the temperature of Li-ion batteries must be maintained below 40 °C with deviations of less than 5 °C [24,25]. In the last two decades, considerable research has been performed on battery thermal management systems, including air cooling with natural convection and forced convection [26,27], indirect liquid cooling with cold plates or heat pipe [28], and direct-immersion cooling [29], and cooling with phase change material. [30] Kalkan et al. [31] experimentally demonstrated that natural convection with air cooling led to high temperatures of 52 °C at a 5C-rate owing to the low heat transfer coefficient (HTC). To improve the HTC, Wang et al. [32] implemented forced convective cooling with air. However, temperatures approaching 40 °C were observed in certain cases, revealing inadequate cooling performance. Despite numerous research efforts, it has been challenging to achieve a target temperature of less than 40 °C [33,34]. To enhance the cooling performance, the research focus has shifted toward liquid cooling, which offers higher HTCs than air cooling. Among various liquid cooling strategies, the predominant approach has been indirect forced convection cooling using a cold plate, given its ease of implementation. For example, Shen et al. [35] adopted a microchannel cold plate with water as the working fluid and demonstrated that the maximum temperature was maintained below 38 °C under a discharge rate of 5C. Zhao et al. [36] enhanced the temperature uniformity in a battery pack by approximately 3 °C using serpentine channel flow with a water–methanol mixed coolant. However, indirect liquid cooling is associated with a high thermal resistance [37] owing to the inclusion of thermal interfacial materials (TIMs) to attach the cold plate to the battery [38,39]. Thus, researchers have studied direct liquid cooling strategies to eliminate the increased thermal resistance caused by TIMs. Wu et al. [40] conducted experiments involving direct-immersion cooling using NOVEC 7000, which could maintain temperatures below 36 °C under a 4C-rate discharge condition. Through an experimental investigation, Hirano et al. [41] showed that the incorporation of porous materials and microfibers between battery cells to enhance boiling resulted in a temperature reduction of approximately 44 °C compared with air cooling, in a 20C charge–discharge cycle. However, research on enhancing cooling performance through battery surface modifications remains limited. Existing studies have predominantly focused on active cooling methods, such as forced convection with cooling plates. Recently, certain researchers have explored immersion cooling directly applied to the battery. [42–44] Nonetheless, immersion cooling on smooth surfaces requires a significantly high superheat for boiling incipience. This requirement leads to rapid temperature drops upon boiling incipience, resulting in battery instability. Given the continuous increase in battery energy density, it is necessary to identify methods to lower the required temperature of boiling incipience, thereby effectively improving the boiling cooling performance.

Nano-engineered surfaces, featuring a porous structure, offer numerous nucleation sites that decrease the superheat required for the onset of boiling (ONB), thereby mitigating thermal shock during operation. Furthermore, the increased surface area promotes boiling heat transfer [45]. Lee et al. [46] demonstrated that a surface with porous copper can enhance the critical heat flux (CHF) by up to 185% compared with that of a bare silicon surface. Yao et al. [47] revealed that a nanowire surface structure resulted in a two-fold increase in the CHF relative to a smooth surface. Li et al. [48] showed that the implementation of surface treatment to generate appropriately sized cavities can lower the ONB temperature by 23 °C…

2. Experimental method

The objective of this study was to establish a direct immersion cooling solution using an LIG-coated surface. In order to access the thermal performance of the LIG-coated lithium-ion battery, we outline the overview of the test section's design, encompassing the fabrication process of the LIG, as well as the experimental procedure and measurement accuracy.

2.1. LIG fabrication

LIG was selected for enhancing the immersion cooling of lithium-ion batteries due to its facile fabrication process, which is conducive for large-scale production. In general, the process of preparing LIG involves the irradiation of polymers with carbon dioxide laser, which triggers localized high temperatures within the polymer structure. This high-temperature environment induces instantaneous transformation of the polymer, such as polyimide, into graphene. This process, known as pyrolysis, facilitates the conversion of the polymer into three-dimensional porous carbonaceous materials. Specifically, when polyimide is subjected to laser irradiation, it undergoes rapid conversion into graphene, resulting in the formation of LIG. [49] LIG exhibits a significantly larger specific surface area of 340 m^2/g compared with that (0.0055 m^2/g) of pristine polyimide film [50], and its thermal conductivity k (13 W/m·K)

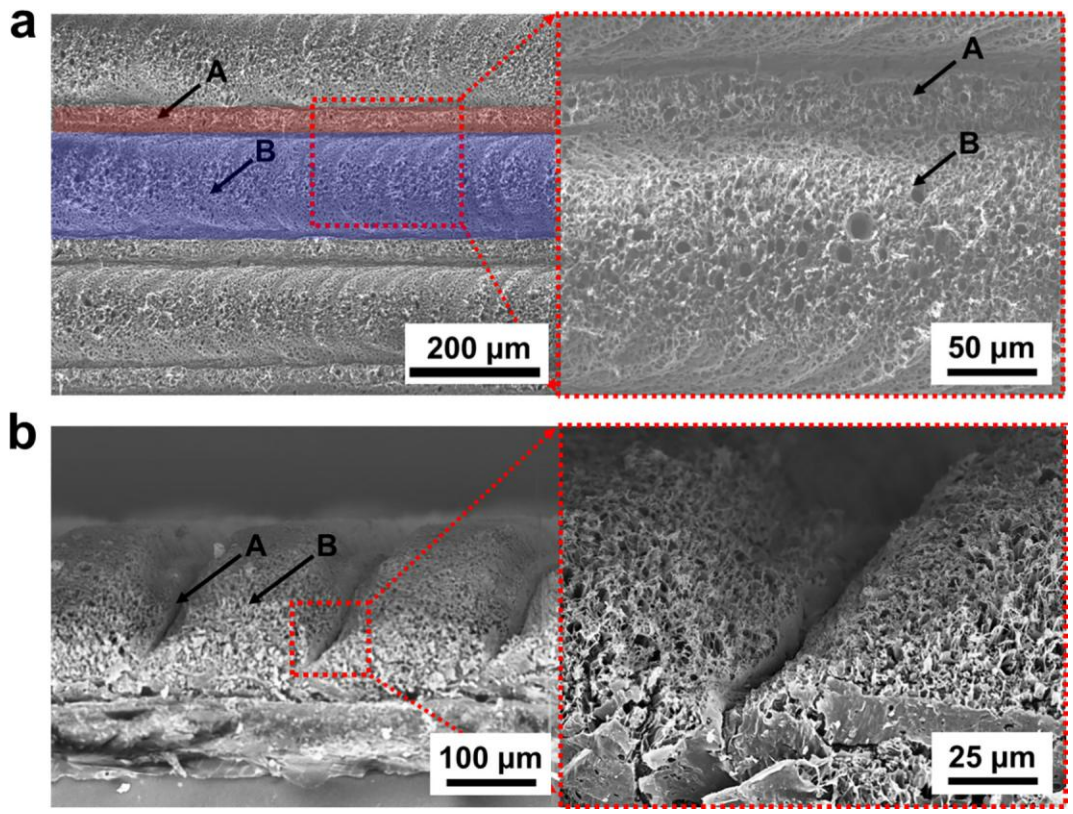

Fig. 2. SEM image of microfabricated LIG. (a) Top view and (b) side view of LIG fabricated with 14.5% of the maximum power, irradiation speed of 200 mm/s, and an irradiation interval of 200 μm. Region A exhibits valley-like LIG with a thickness of 25 μm, whereas Region B displays hill-like LIG with a thickness of 50 μm.

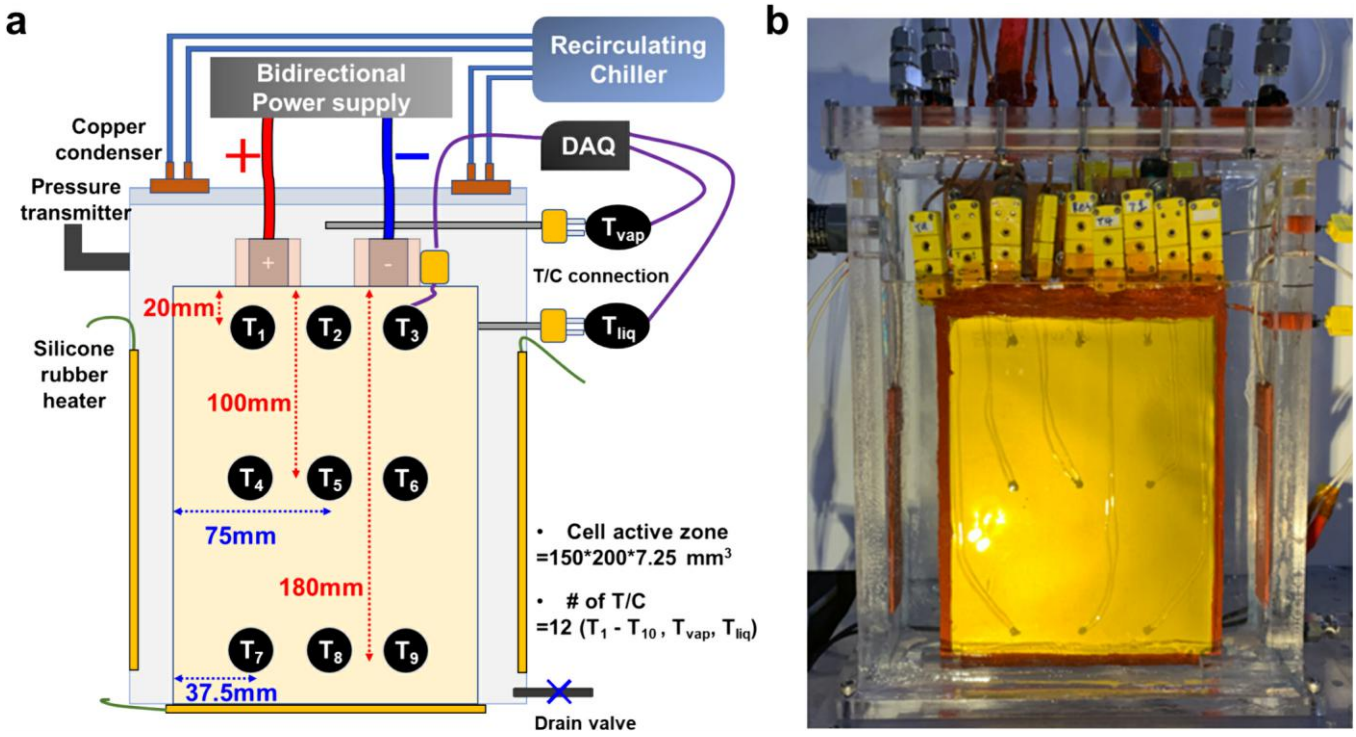

Fig. 3. Experimental setup. (a) Experimental Schematic. (b) Image of experimental setup. A bidirectional power supply was used to operate the battery, and internal coolant condensation was achieved using a recirculating chiller. Additionally, data were obtained using 10 thermocouples, a pressure sensor, a data acquisition system (DAQ), and bidirectional power supply.

is approximately two orders of magnitude higher than that of pristine polyimide (0.15 W/m·K) [51].

Fig. 1 illustrates the process of fabricating LIG on the battery surface. A battery sized 160 × 227 × 7.25 mm^3 was covered by a 70-μm-thick conventional polyimide film, followed by direct laser irradiation onto the polyimide film. A CO_2 laser system (Coryart Inc., C1060, $\lambda = 10.6$ μm) with a maximum power of 80 W was used to fabricate LIG over a 150 × 200 mm^2 area of the battery surface, corresponding to the size of the active material involved in the electrochemical reactions for generating electrical current. Before the thermal testing, the laser system for LIG fabrication was characterized, considering factors such as the laser power (10–30% of the maximum value), scanning speed (50–300 mm/s), and irradiation interval (100–400 μm), to identify the ideal operating conditions for obtaining high-quality LIG without damaging the adhesive or battery layers. Subsequently, the quality of the produced LIG was evaluated by scanning electron microscopy (SEM) and Raman spectroscopy. Results indicated that the optimal conditions involved a laser scanning speed of 200 mm/s, maximum laser power of 14.5%, and an irradiation interval of 200 μm per line.

Fig. 2 shows the SEM images of the fabricated LIG under the optimal laser operating conditions. The images show a consistently formed microporous structure over the active material portion. Specifically, Region A (marked with a red box) reveals graphene formation in a valley-like shape with an approximate thickness of 25 μm. Conversely, in Region B (marked with a blue box), a thicker hill-like graphene layer with a thickness of approximately 50 μm can be observed due to the concentration of laser power along the irradiated laser path, accompanied by nanowire structures on the top of the LIG. A more comprehensive SEM image of the LIG can be found in Fig. S1.

2.2. Experimental setup and test procedure

Fig. 3 shows a schematic and the image of the experimental setup. The chamber, with dimensions of 210 × 270 × 70 mm^3, included 15-mm-thick acrylic plates. A pressure transmitter (Trafag, EPI 8287) was installed at the top of the chamber to measure the internal pressure, and two K-type thermocouples (Omega, KMQSS-062G-6) were inserted to measure the air and bulk fluid temperatures, respectively. To determine the surface temperature of the battery cell, 125-μm-diameter K-type thermocouples (Omega, Chal-005) were affixed at ten distinct locations beneath either the polyimide film or LIG layer. Nine points, labeled T_1–T_9, were defined to examine the temperature uniformity on the front surface of the battery, as illustrated in Fig. 3(a), and an additional point was identified on the backside to check the symmetry on both sides. Points T_1 to T_3 were positioned 20 mm below the battery electrodes. T_4 to T_6 were placed at the midsection, 100 mm from both the top and bottom ends. T_7 to T_9 were located 20 mm from the bottom end, mirroring the locations of T_1 to T_3. T_{10} corresponded to the identical location as T_5, but on the opposite side and in the center. In the horizontal direction, measurements at T_1, T_4, and T_7 were obtained 37.5 mm from the left side; T_2, T_5, and T_8 were located at the center line; and T_3, T_6, and T_9 were located 37.5 mm from the right side.

During thermal testing under standard environmental conditions, the fluid inside the chamber was maintained at 20 °C. For testing under harsh environmental conditions, the fluid was maintained at 33.5 °C by using silicone rubber heaters attached to the sides and bottom of the chamber. Two copper blocks, connected to a recirculating chiller (Jeiotech, RC-05), were inserted at the top of the chamber to maintain a constant fluid temperature, and condense the vaporized fluid back to a liquid state. Consequently, the maximum internal pressure during the tests was 102.2 ± 0.5 kPa, which does not affect the thermophysical properties of working fluid significantly.

The battery cycle process was implemented using a programmable bidirectional power supply (Itech, IT6005C-80-150). Charge, discharge, and relaxation processes were continuously performed using pre-programmed steps based on the LabVIEW algorithm. Experimental data logging was initiated once the fluid temperature inside the chamber stabilized at the desired steady-state temperature. A large-format prismatic LFP battery (A123 systems, AMP20M1HD-A) with a capacity of 20 Ah and an LFP cathode was used in the experiments. The specifications of this battery are listed in Table 1. Before the thermal test, the actual capacity was determined by performing four charge–discharge cycles at a rate of 0.5C, assuming an initial capacity of 20 Ah. Data of the first charge–discharge cycle were excluded to eliminate side-reaction effects, such as the initial capacity state and solid electrolyte interphase (SEI) layer formation. Subsequently, the actual capacity of the battery, Q_{act}, was calculated through Eq. (1), using data from the second to fourth discharge cycles, and the actual C-rate was determined using Eq. (2). In this analysis, the actual battery capacity was measured to be 19.87 Ah, obtained by averaging three repeated capacity measurements. All cycle tests, including initial capacity calculation and thermal experiments, were conducted using a preset constant current (CC)–constant voltage (CV) charge and CC discharge protocol, as described in Supplementary Note 1.

$$\text{Capacity (Ah)} : Q_{act} = \frac{1}{3600}\int_0^t i_{\text{discharge}}\,dt \tag{1}$$

$$\text{C} - \text{rate} : \text{C-rate} = \frac{\frac{1}{t}\int_0^t i_{\text{discharge}}\,dt}{Q_{\text{act}}}, \tag{2}$$

Five cases were designed for testing: Thermal tests were conducted using two working fluids, air (Case 1) and HFE-7000 (Cases 2–5). In Cases 1–3, a constant temperature of 20 °C was maintained, simulating standard environmental conditions, whereas a temperature of 33.5 °C was maintained in Cases 4–5, simulating harsh environmental conditions. Moreover, a comparative analysis was performed between batteries with polyimide-coated (Cases 1, 2, and 4) and LIG-coated surfaces (Cases 3 and 5). Notably, in the case of immersion cooling (Cases 2–5), the complete chamber is not filled with HFE-7000 owing to a potential gap at the connection point between the battery tap and active zone. Specifically, during immersion cooling, the battery is immersed in HFE-7000 only up to the active zone below the tab. At the beginning of the experiment, the volume of liquid is approximately 1.44 L. Table 2 summarizes the experimental cases. The thermophysical properties of the working fluids are presented in Table S1.

Table 1
Specifications for 20 Ah LiFePO4 battery.

Cathode material	$LiFePO_4$
Anode material	Graphite
Electrolyte	Carbonate based
Cell total dimensions [mm^3]	7.25 × 160 × 227
Cell active zone [mm^3]	7.25 × 150 × 200
Cell weight [g]	496
Cell capacity [Ah]	20
Minimum cell capacity [Ah]	19.6
Operating voltage [V]	2–3.5
Nominal voltage [V]	3.3
Nominal energy [Wh]	65
Nominal specific energy [Wh/kg]	131
Nominal specific energy density [Wh/L]	247
Nominal discharge power [W]	1200
Nominal specific power [W/kg]	2400

Table 2
Experimental conditions, coolant, and surface type for battery cooling.

Case number	Coolant	Temperature (°C)	Surface material
Case 1	Air	20	Polyimide
Case 2	HFE-7000	20	Polyimide
Case 3	HFE-7000	20	LIG
Case 4	HFE-7000	33.5	Polyimide
Case 5	HFE-7000	33.5	LIG

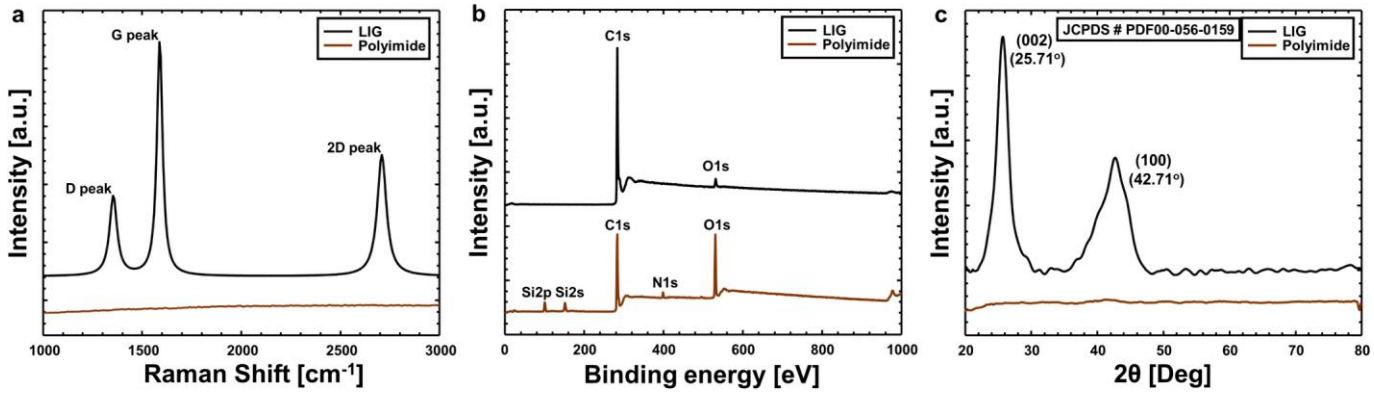

Fig. 4. Surface characterization of pristine polyimide and LIG. (a) Raman spectroscopy, (b) X-ray photoelectron spectroscopy, and (c) X-ray diffraction results of pristine polyimide and powdered LIG. The results of all three surface analysis methods indicated the high quality of LIG and its suitability for use in subsequent experiments.

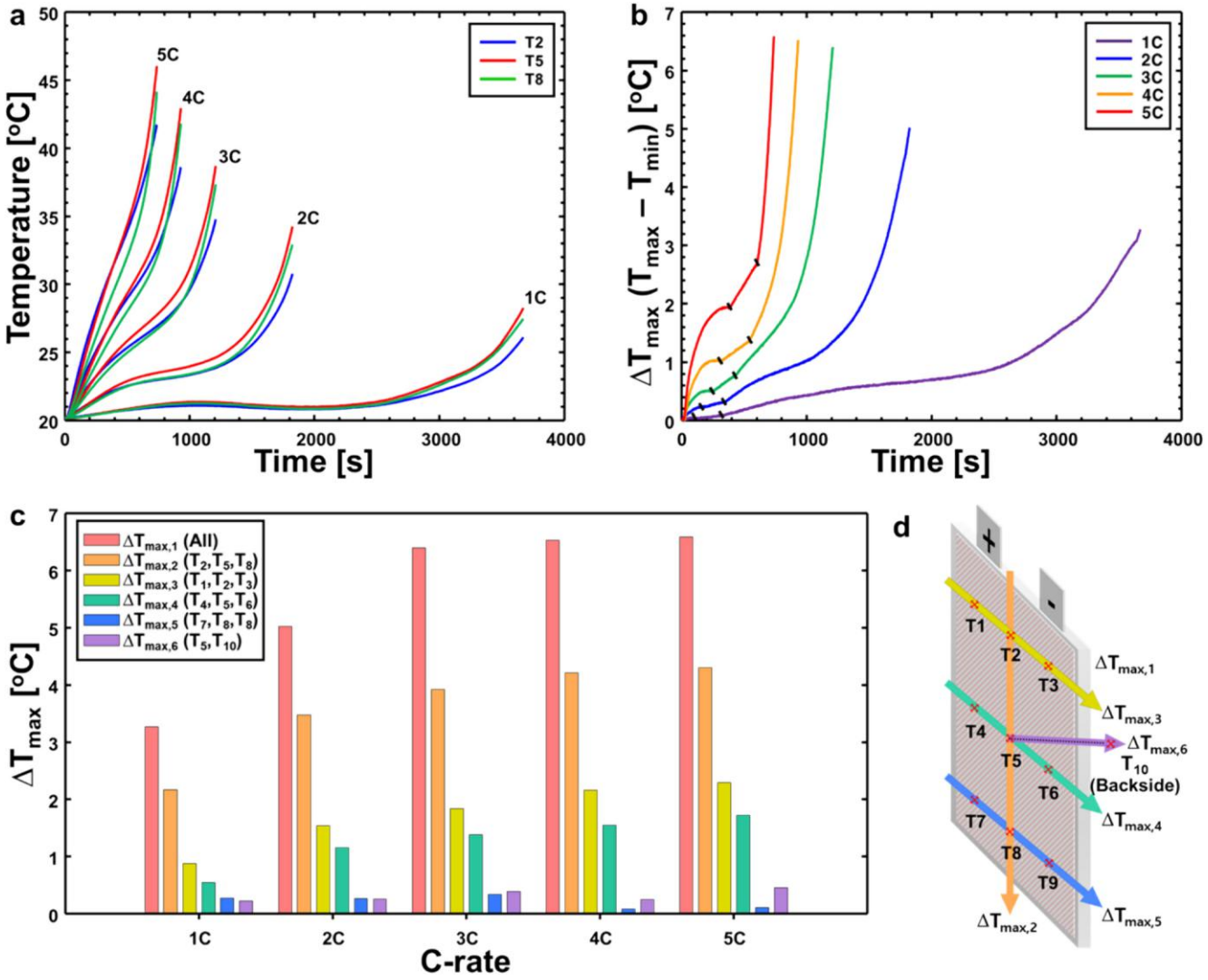

Fig. 5. Temperature variation over time in the case of air cooling at $T_f = 20$ °C under 1–5C-rate discharge conditions (Case 1). (a–b) local temperature profiles and maximum temperature difference of pristine polyimide surface. (c) Maximum temperature difference on all surfaces and at the vertical, horizontal, and symmetric positions (d) Temperature difference at different locations. Case 1 exhibited high temperatures and low temperature uniformity, necessitating the implementation of appropriate cooling strategies.

2.3. Experimental accuracy

The surface temperature (measured by the thermocouples), absolute pressure (measured using a pressure transmitter), and voltage and current were simultaneously monitored using the data acquisition module (National Instruments, NI 9214), digital multimeter (Keithley Instruments, Keithley 2000), and programmable bidirectional power supply (Itech, IT6005C-80-150), respectively. All collected data were integrated and synchronized through the LabVIEW program, with data points recorded at a rate of one per second. The K-type thermocouples used to measure the battery surface and fluid temperatures had an accuracy of ±0.4%. The pressure transmitter for system pressure measurements had an accuracy of ±0.5%. The bidirectional power supply had an accuracy of 0.02% + 0.02% over the full scale for voltage and 0.1% + 0.1% over the full scale for current. Temperature data were consolidated through DAQ NI 9214 with an accuracy of 0.01 °C, while pressure data were gathered using Keithley 2000 with an accuracy of 10 μA. Table S2 summarizes the accuracy values of the measurement equipment and calculated uncertainty, as suggested by Moffat et al. [52]

3. Results and discussion

A surface analysis was performed to quantitatively assess the quality of the produced LIG. Specifically, Raman spectroscopy, X-ray photoelectron spectroscopy (XPS), and X-ray diffraction (XRD) analyses were performed to examine the LIG surface. Subsequently, the thermal behaviors of the battery in the five cases were experimentally evaluated.

3.1. LIG surface characterization

Surface characterization was performed both before and after LIG generation to evaluate its quality before being subjected to thermal testing. The results are shown in Fig. 4. The surface analysis involved three techniques: Raman spectroscopy (Weve, Inc., wavelength = 531 nm, laser power = 0.3 mW), XPS (Thermo Fisher Scientific, Inc., spot size = 400 μm), and XRD (Bruker-AXS, Inc., wavelength = 1.54 Å).

According to the literature, LIG exhibits three main peaks: near 1350 cm^{-1} (D peak), 1580 cm^{-1} (G peak), and 2700 cm^{-1} (2D peak) [50,51,53]. The intensity ratio of the D peak to the G peak (I_D/I_G) is commonly used to assess the quality of the graphene structure and presence of defects, with a lower ratio indicating a well-formed graphene structure. In this study, as shown in Fig. 4(a), the D peak was observed at 1354 cm^{-1}, whereas the G peak and 2D peak appeared at 1583 cm^{-1} and 2705 cm^{-1}, respectively. The I_D/I_G value for the LIG was calculated to be 0.19, indicating the production of graphene structures with minimal defects. Details of the Raman data at different points are presented in Fig. S2.

Fig. 4(b) shows a comparison of the XPS data obtained from pristine polyimide and LIG. In the XPS spectrum of pristine polyimide, peaks corresponding to various elements could be observed, including a C1s peak at 283.9 eV; an N1s peak at 399.2 eV; an O1s peak at 531.2 eV; and Si2s and Si2p peaks at 101.3 eV and 152.1 eV, respectively. The N1s peak was attributable to the nitrogen in polyimide's atomic structure, and Si2s and Si2p peaks were associated with the silicon adhesive layer. The XPS data of LIG revealed similarities in the C1s and O1s peaks (284.2 eV and 532.1 eV, respectively) compared with pristine polyimide. However, the intensities of the C1s and O1s peaks were higher and lower than those of pristine polyimide, respectively. These changes could be attributed to the formation of graphene layers during LIG growth, indicating of well-formed LIG [54,55]. Additionally, as graphene growth progressed, the N1s, Si2s, and Si2p peaks were not observed in the XPS spectra.

The XRD spectra indicated peaks at 2θ = 25.7° and 42.7° after the formation of LIG, as depicted in Fig. 4(c). These peaks were absent in the spectra of pristine polyimide. The presence of peaks corresponding to the (002) and (100) structures of graphite (JCPDS card number 00–056-0159) indicates the occurrence of carbonization from polyimide to LIG [50,54,56].

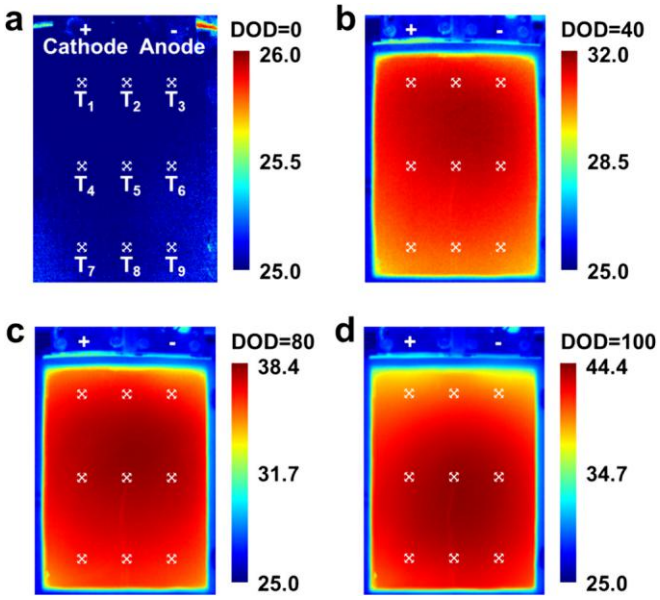

Fig. 6. Infrared thermal camera images recorded in the discharge process under 25 °C. Sequential thermal images were obtained to examine the transient temperature distribution at 4C-rate discharge at different depths of discharge (DOD): (a) 0%, (b) 40%, (c) 80%, and (d) 100%. These images validated the temperature uniformity results for Case 1.

3.2. Battery thermal behavior and cooling experiments

3.2.1. Thermal behavior evaluation under $T_f = 20$ °C air cooling

Before evaluating the performance of immersion cooling, the thermal behavior associated with air natural convection with an ambient temperature of $T_f = 20$ °C (Case 1) was analyzed. This case served as a reference to compare the thermal characteristics of the LFP battery with other cases. The objective of the thermal tests was to evaluate the increase in the overall temperature and temperature variations at different locations on the battery surface during the discharge condition.

Fig. 5 illustrates the thermal behavior during discharge at 1–5C-rates for Case 1. Fig. 5(a) shows the temperature increase on the vertical centerlines (T_2, T_5, T_8). The highest temperatures for 1–5C-rates were 28.5 °C, 34.3 °C, 39.4 °C, 43.1 °C, and 46.1 °C, respectively. Notably, as the C-rate increased from 1C to 5C, the temperature increase became less significant, with $\Delta T_{1C\text{-}2C} = 5.8$ °C to $\Delta T_{4C\text{-}5C} = 3.0$ °C. This behavior can be attributed to two key reasons: 1) The ionic mobility increases as the battery temperature rises, leading to reduced internal electrical resistance and heat generation; and 2) at higher C-rates, higher surface temperatures lead to a stronger natural convective heat transfer than that at lower C-rates.

Fig. 5(b) shows the maximum temperature difference across nine points on the battery surface during the discharge condition. In the early stages of discharge, the highest temperature was observed in the upper part ($T_{1–3}$), which is closer to the tab, with slightly higher values on the cathode side ($T_1 > T_3$). This phenomenon occurred because of the higher current density on the positive tab side [57]. As discharging continued, the maximum surface temperature gradually shifted toward the middle and lower end of the battery, and the temperature difference became more pronounced. This behavior occurred because of the transient utilization of the active material, which initiated at the region near the tab and progressed downward [40]. Consequently, the temperature difference changed over time. Initially, the maximum difference was observed between $T_{1–3}$ and $T_{7–9}$. Subsequently, the maximum temperature difference shifted to that between $T_{4–6}$ and $T_{7–9}$ and finally to that between

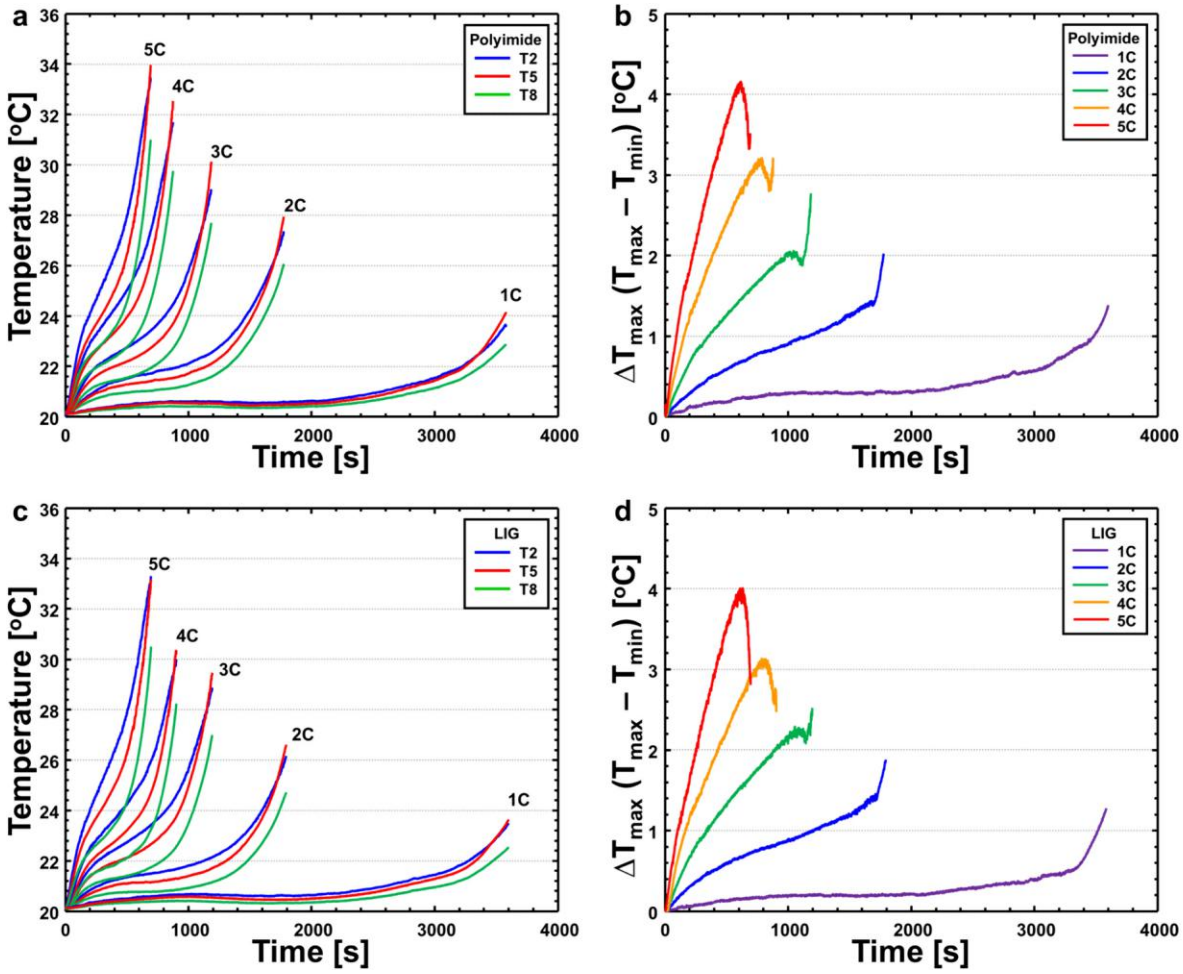

Fig. 7. Temperature behavior under $T_f = 20$ °C immersion cooling (Cases 2 and 3). (a–b) Local temperature profiles and maximum temperature difference of pristine polyimide surface. (c–d) Local temperature profiles and maximum temperature difference of LIG surface. Cases 2 and 3 exhibited improved cooling performance compared with Case 1. The battery coated with LIG (Case 3) exhibited higher cooling performance to that achievable using pristine polyimide.

$T_{4–6}$ and $T_{1–3}$. These results indicated that air cooling is insufficient for discharge rates exceeding 3C, because the maximum operating temperature of the battery must not exceed 40 °C and the temperature uniformity must be within 5 °C [24,25].

Fig. 5(c) and (d) illustrates the temperature uniformity in terms of the maximum temperature difference along the vertical center ($\Delta T_{max,2}$), the three horizontal lines ($\Delta T_{max,3}$, $\Delta T_{max,4}$, $\Delta T_{max,5}$), and center points of the front and back sides ($\Delta T_{max,6}$). The highest temperature difference was observed in the vertical direction, owing to the transient shift of the maximum heating region toward the lower region as discharging progresses. The temperature differences in the horizontal direction were smaller than that along the vertical centerline. Among the three horizontal lines, $\Delta T_{max,3}$ exhibited the largest temperature difference due to larger heat generation near the cathode. The agreement between T_5 (front center) and T_{10} (back center) (difference of less than within 0.45 °C) demonstrated the symmetry in the temperature variations.

To validate the temperature uniformity during discharging conditions, sequential infrared thermal images at a 4C-rate were recorded while maintaining the external air temperature of 25 °C. The surface of the battery was coated with pre-calibrated black paint (emissivity = 0.93), and the results are depicted in Fig. 6. The analysis was based on four depths of discharge (DODs): 0, 40%, 80%, and 100%, calculated using Eq. (3). Initially, the maximum surface temperature was observed near the tab until the DOD reached 40%. Additionally, the higher temperature observed on the cathode side in Fig. 6(b) indicated increased heat generation compared with that on the anode side. However, as the DOD increased to 80% and 100%, the maximum surface temperature appeared near the middle and bottom regions, as shown in Fig. 6(c) and (d). This result validated the results of temperature uniformity for Case 1.

$$\text{Depth of discharge}: DOD(\%) = \left(\frac{1}{3600 Q_{act}} \int_0^t i_{discharge} dt\right) \cdot 100 \quad (3)$$

3.2.2. *Immersion cooling with polyimide and LIG surfaces under room temperature*

In this analysis, we evaluated the thermal behavior of an immersion-cooled battery using HFE-7000 as the coolant. For comparison, batteries with pristine polyimide (Case 2) and LIG (Case 3) surfaces were considered. Fig. 7 shows the change in the surface temperature and maximum temperature difference over time during 1 to 5C-rate discharge conditions for the two surfaces. Similar to air cooling, the surface temperature of the pristine polyimide battery under immersion cooling with HFE-7000 (Case 2) gradually increased over time. However, the maximum temperatures during immersion cooling (24.2 °C, 27.9 °C, 30.1 °C, 32.5 °C, and 34.0 °C for rates of 1–5C, respectively) were 4.1–12.1 °C lower than those observed during air cooling. Additionally, the maximum temperature differences at rates of 1–5C were 1.5 °C, 2.0 °C, 2.8 °C, 3.2 °C, and 4.2 °C, respectively. Notably, the maximum temperature difference under the 5C-rate decreased from 6.6 °C for air cooling to 4.2 °C for HFE-7000-based immersion cooling.

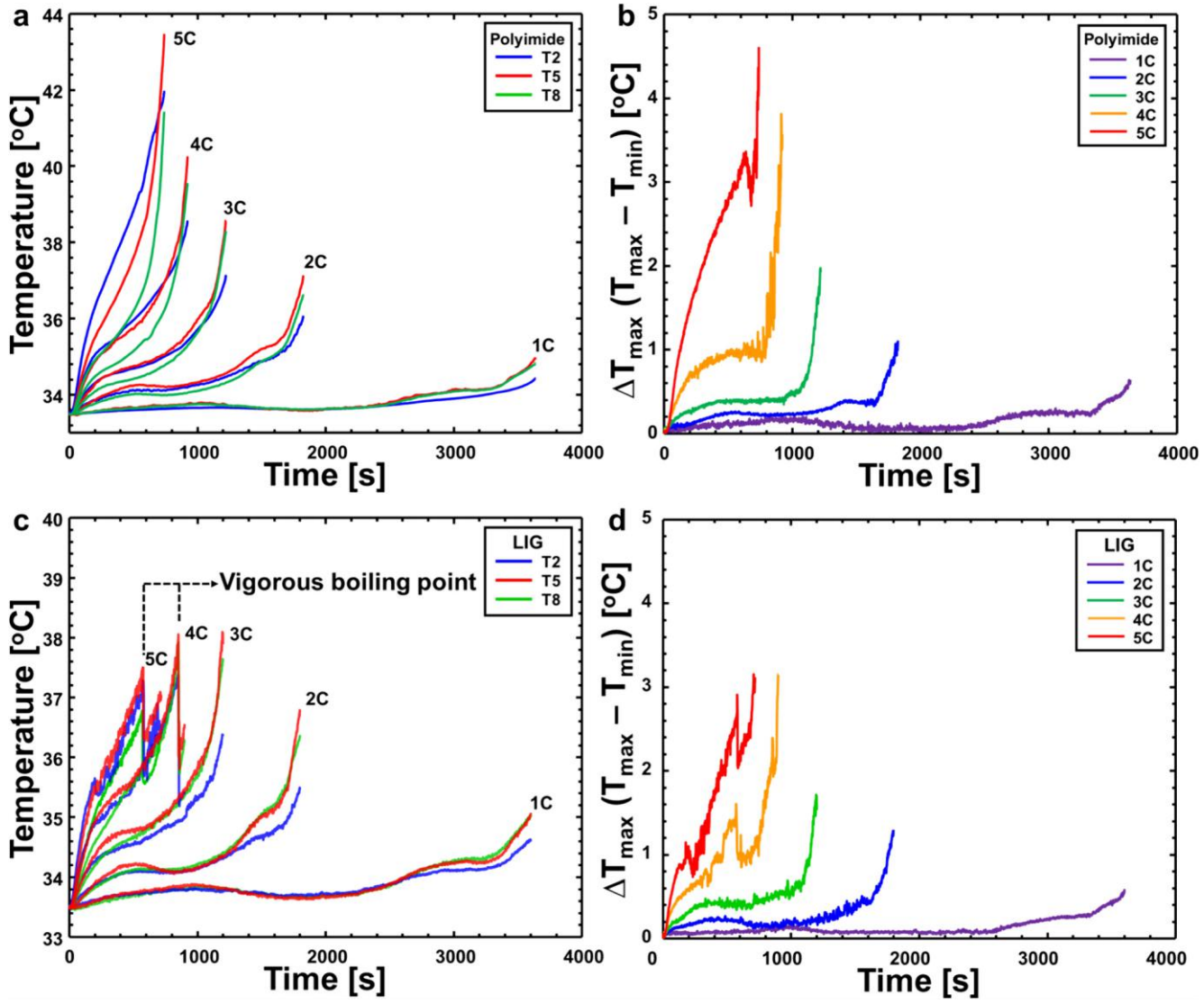

Fig. 8. Temperature behavior during immersion cooling at $T_f = 20$ °C (Cases 4 and 5). (a–b) Local temperature profiles and maximum temperature difference of pristine polyimide surface. (c–d) local temperature profiles and maximum temperature difference of LIG surface. At high environmental temperatures, the polyimide surface battery (Case 4) exhibited inadequate cooling performance. In contrast, the LIG-coated battery (Case 5) demonstrated outstanding performance owing to the surface boiling effect.

In the case of immersion cooling using the LIG-coated battery (Case 3), the cooling performance was further enhanced, with maximum temperatures of 23.6 °C, 26.6 °C, 29.5 °C, 30.4 °C, and 33.4 °C for 1–5C-rates, respectively. These values are 4.6–12.7 °C lower than those of air cooling and 0.5–2.1 °C lower than those for immersion cooling on the pristine polyimide surface. The superior thermal performance of LIG is attributable to the increased surface area resulting from its porous structure and improved thermal conductivity compared with polyimide. Furthermore, the maximum temperature differences were 1.4 °C, 1.9 °C, 2.5 °C, 3.1 °C, and 4.0 °C at rates of 1–5C, up to 3.9 °C lower than air cooling and up to 0.3 °C lower than those in Case 2. The slight difference between pristine polyimide and LIG arises from the absence of boiling incipience due to the low fluid temperature.

For both surfaces, the thermal behavior of immersion cooling differed from that of air cooling. In the case of air cooling, the maximum temperature shifted from the top end to the middle-bottom region during discharge. However, in the case of immersion cooling, the chamber was not fully filled with HFE-7000; instead, it was filled to a level below the battery tab. Thus, the active zone was cooled using HFE-7000, whereas the area near the tab was cooled using air. This configuration was unlike Case 1, in which all parts of the battery were cooled solely by air. Consequently, the temperatures of $T_{1–3}$, situated closer to the tab, were consistently higher than those of $T_{7–9}$. As a result, the trend of the maximum temperature difference varied. The highest temperature difference value was observed when the temperature difference between T_2 and T_8 was the highest and gradually decreased as the temperature of T_8 increased.

3.2.3. Two-phase cooling with LIG surface under harsh environmental conditions

In general, batteries are used in diverse environmental conditions, and inadequate cooling under high environmental temperatures can accelerate the formation of the SEI layer, which may trigger premature TR [58]. Thus, we evaluated the effectiveness of immersion cooling using pristine polyimide and LIG coated batteries under a high environmental temperature of $T_f = 33.5$ °C, which is close to the saturation temperature of HFE-7000 under atmospheric pressure. Fig. 8 depicts the thermal behavior associated with immersion cooling using pristine polyimide (Case 4) and LIG (Case 5) surfaces at $T_f = 33.5$ °C. In the case of the pristine polyimide surface, the maximum surface temperature was

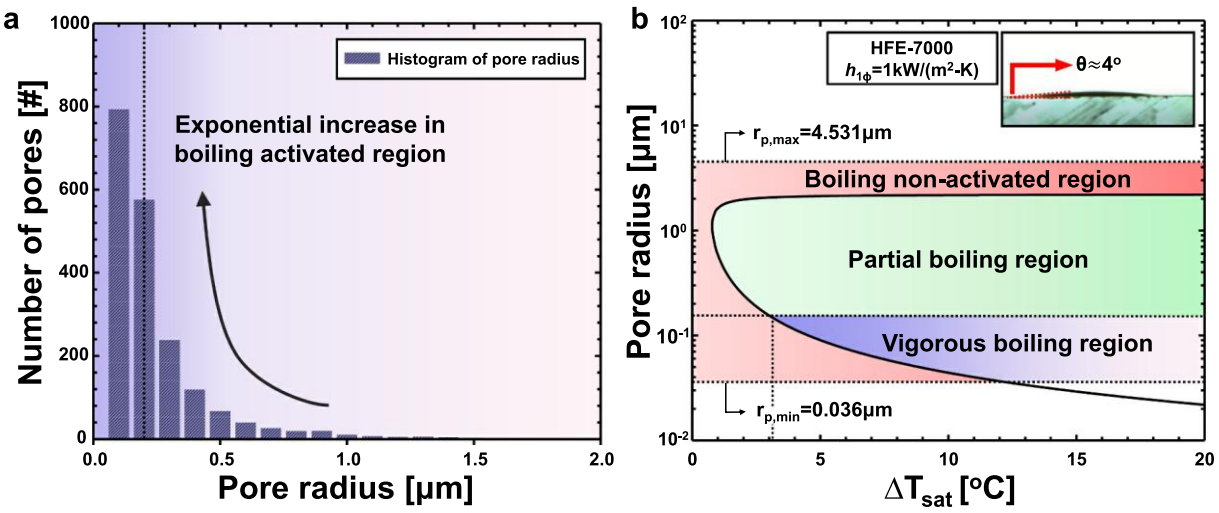

Fig. 9. Relation between surface pore radius and boiling characteristics and Hsu model calculations. (a) Statistical analysis of pore size distribution; (b) required wall superheat temperature ΔT_{sat} for different activated nucleation pore radii, according to the Hsu model. The LIG pore radius distribution and Hsu model results were used to examine the onset of nucleate boiling (ONB) and corresponding rapid temperature decrease.

43.5 °C, and the highest temperature difference was 4.6 °C during 5C-rate discharging, as shown in Fig. 8(a) and (b). The temperature rise was lower than that when HFE-7000 was used at $T_f = 20$ °C (Case 2) owing to the less generation at higher environmental temperatures due to the low internal resistance of the battery. However, the maximum temperature exceeded 40 °C owing to the higher fluid temperature, which was not favorable for battery operation. Notably, although the surface temperature exceeded the saturation temperature, no boiling was observed at any C-rate. This is likely due to the pristine surface and hydrophilic nature of HFE-7000, which hinders ONB and requires a large superheat temperature to initiate boiling. The temperature difference for Case 4 is shown in Fig. 8(b). Consequently, the maximum temperature trend was similar to that in the case of air cooling, and as discharging progressed, the temperature difference increased rapidly.

The thermal performance results for the LIG-coated battery (Case 5) are shown in Fig. 8(c) and (d). Superior cooling performance was observed: The maximum temperature was 37.8 °C at a 5C-rate, and the maximum temperature difference was maintained below 3.2 °C. At 1C-rate, the maximum temperature reached 35.1 °C, exhibiting a trend similar to that of the pristine polyimide surface. In contrast, at high discharge rates (2C or more), the cooling performance was significantly improved, with a temperature decrease of up to 5.7 °C compared with that for the pristine polyimide surface. This enhancement was attributable to nucleate boiling on the LIG surface. The micropores in the LIG functioned as vapor embryo for bubble nucleation, and thus, ONB occurred at a lower superheat temperature, thereby promoting boiling heat transfer. The required superheat for boiling (ΔT_{sat}) for vigorous boiling, defined as the difference between the surface and saturation temperatures, was approximately 3.2–3.8 °C at rates of 4–5C, evident from the surface temperature oscillation near $T \sim 3.75$–38.0 °C, as shown in Fig. 8(c).

Fig. 9 shows the radius distribution of the porous structure on the LIG surface and corresponding required superheat for ONB. Boiling did not occur at the 1C-rate, partial boiling occurred at rates of 2–5C, and vigorous boiling occurred over the surface at rates of 4 and 5C. These outcomes were closely related to the pore size of LIG and ΔT_{sat}. Fig. 9(a)

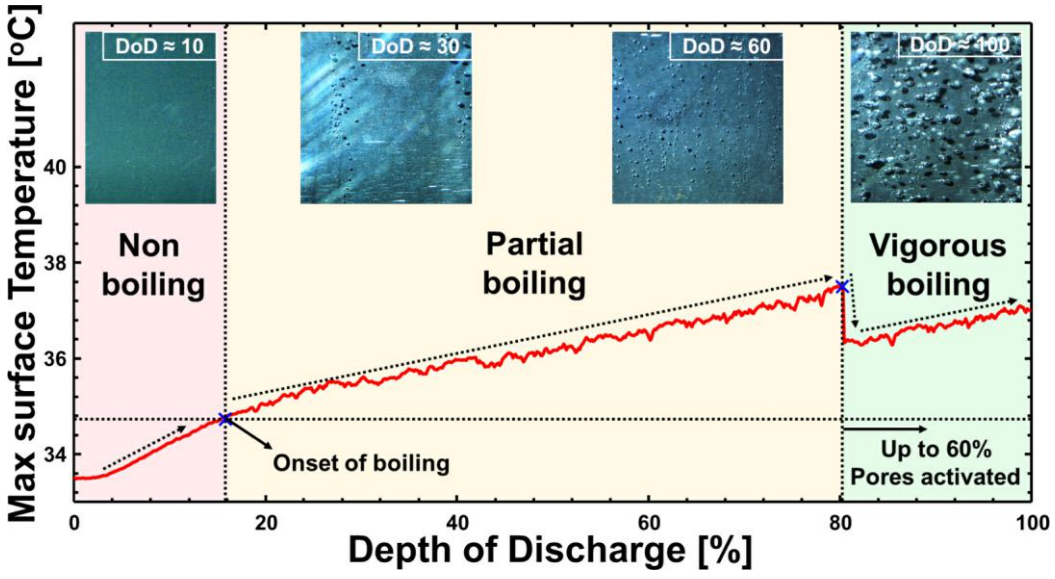

Fig. 10. Maximum temperature profile for different DODs of LIG-coated battery during 5C-rate discharging, with corresponding bubble dynamics images. In the early stages, local nucleate boiling and data oscillation were observed. Subsequently, a significant number of pores became involved in boiling, leading to rapid temperature reduction and emergence of numerous bubbles.

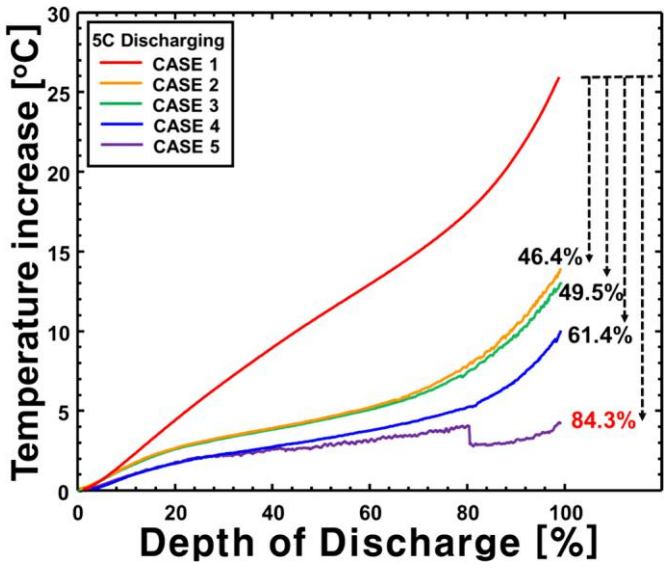

Fig. 11. Comparison of thermal behaviors under five different cooling schemes. The figure presents the maximum temperature increase in the five schemes under the 5C-rate discharging condition. The LIG-coated battery demonstrates superior cooling performance compared with that of the battery including the polyimide film, especially under high environmental temperatures and discharge rates.

shows the pore size distribution on the LIG surface, obtained from SEM data using the open-source image analysis software ImageJ. The pore radius ranged from 0.04 to 4.53 μm, and the number of pores rapidly increased as the pore radius decreased. Note that pores with radii of or greater than 2 μm are not shown in the figure, as their effect on boiling onset was considered negligible based on calculations using the Hsu model [59], and they were not present in large numbers. Pores with a radius of 0.15 μm or less accounted for approximately 60% of the total. Using these findings, the Hsu model was applied to establish the relationship between the pore radius and ΔT_{sat}.

$$\text{Hsu model}: \{r_{p,min}, r_{p,max}\} = \frac{\delta_t}{2}\left(\frac{sin\theta}{1+cos\theta}\right)\left(1 \mp \sqrt{1-\frac{8\sigma(1+cos\theta)T_{sat}}{h_{fg}\rho_g \Delta T_{sat}\delta}}\right), \quad (4)$$

where θ, σ, ρ_g, and h_{fg} denote the contact angle, surface tension, vapor density, and latent heat of HFE-7000, respectively. δ_t is the thickness of the thermal boundary layer and can be simply obtained from $k_l/h_{1\phi}$, where k_l is thermal conductivity of HFE-7000 and $h_{1\phi}$ is the single-phase natural convection HTC. The required ΔT_{sat} for ONB for different pore radii is shown in Fig. 9(b). As ΔT_{sat} increased, the area in which boiling is initiated gradually expanded. When ΔT_{sat} reached 3 °C or higher, the proportion of activated pores exceeded 60%. Consequently, as the surface temperature of the battery increased, the number of activated pores exponentially increased. Once boiling was activated in a pore with a radius of 0.15 μm or less, it instantaneously spread to numerous neighboring pores, resulting in a sharp decrease in the temperature at rates of 4 and 5C.

Fig. 10 shows the maximum temperature profile of 5C-rate and corresponding bubble images for different DODs of the LIG-coated battery. High-speed images were captured at 2000 fps with a resolution of 896 × 896 pixels using a Photron FASTCAM Mini UX100. Before boiling initiated, the temperature rapidly increased, and local temperature oscillations occurred with the onset of partial boiling. Once boiling was initiated over the LIG surface, a large number of bubbles were observed, leading to a substantial temperature drop. Furthermore, even under high C-rate discharge conditions, the LIG surface demonstrated excellent heat transfer performance due to the enhanced nucleate boiling heat transfer, which amplified with increasing C-rate. Consequently, the LIG-coated battery exhibited superior cooling performance, resulting in a reduced maximum temperature and more uniform temperature distribution across the battery surface.

Fig. 11 presents a comparison of the maximum temperature increase for all five cooling schemes at the 5C-rate. The cooling performance of HFE-7000 with polyimide surface (Cases 2 and 4) was superior to that of air cooling, as indicated by a 46.4% and 61.4% lower maximum temperature increase under $T_f = 20$ °C and $T_f = 33.5$ °C, respectively. The introduction of the LIG coating further enhanced the cooling performance, with a 49.5% reduction in the maximum temperature rise at $T_f = 20$ °C compared with that of air cooling. Moreover, the LIG-coated surface exhibited remarkable cooling performance, achieving an 84.3% reduction under high environmental temperature conditions of $T_f = 33.5$ °C. This enhancement was attributable to nucleate boiling heat transfer initiated by the porous structure, which resulted in improved temperature uniformity across the entire battery surface.

4. Conclusions

This paper proposes a novel approach for enhancing immersion cooling of LFP batteries through the direct fabrication of LIG on the battery surface. The thermal behaviors of the battery were experimentally evaluated under 1 to 5C-rate discharge conditions by monitoring the changes in the surface temperature. The investigations involved two working fluids, air and HFE-7000, and two fluid temperatures, $T_f = 20$ °C and 33.5 °C. The following conclusions were derived:

(1) Under air cooling at room temperature (Case 1), the maximum temperature at a 5C-rate was 46.1 °C, with the maximum temperature difference being 6.6 °C. The temperature non-uniformity worsened as the maximum temperature region of the battery shifted from the upper region to the lower region as discharging progressed. These results indicate that air cooling is inadequate for battery operation during high C-rate conditions.
(2) Immersion cooling using HFE-7000 at $T_f = 20$ °C (Cases 2 and 3) demonstrated improved cooling performance compared with air cooling. In the case of a polyimide-coated battery surface (Case 2), the maximum temperature and temperature difference were 34.0 °C and 4.2 °C, respectively. When the battery was coated with LIG through laser irradiation (Case 3), cooling was further enhanced, with the maximum temperature and temperature difference being 33.4 °C and 4.0 °C, respectively. This additional enhancement was attributable to the higher thermal conductivity of the LIG and increased surface area resulting from its microporous and nanowire structure.
(3) As the fluid temperature increased to 33.5 °C, approaching the saturation temperature of HFE-7000, the cooling performance of the polyimide surface battery (Case 4) shows deficient, resulting in a maximum temperature of 43.5 °C and maximum temperature difference of 4.6 °C. However, the amount of temperature increase was mitigated by the reduced heat generation at higher operating temperatures.
(4) Immersion cooling with LIG-coated surfaces at $T_f = 33.5$ °C (Case 5) led to enhanced cooling performance through nucleate boiling heat transfer, facilitated by the porous structure of LIG. In particular, the temperature increase was 84.3% lower than that in the case of air cooling (Case 1). Moreover, LIG enhanced the temperature uniformity, as indicated by the maximum temperature difference of 3.2 °C, which is 52% lower than that for air cooling.

CRediT authorship contribution statement

EuiBeen Jung: Data curation, Formal analysis, Investigation, Methodology, Writing – original draft, Writing – review & editing.

Daeyoung Kong: Data curation, Formal analysis, Investigation, Methodology, Writing – original draft. **Minsoo Kang:** Investigation, Methodology. **Juho Park:** Data curation, Investigation, Writing – review & editing. **Jun-Hyeong Kim:** Investigation, Methodology. **Jinho Jeong:** Data curation, Investigation. **Jung Bin In:** Project administration, Supervision. **Ki-Yong Oh:** Project administration, Supervision. **Hyoungsoon Lee:** Funding acquisition, Project administration, Supervision, Writing – review & editing.

Declaration of competing interest

None.

Data availability

Data supporting the results of this study are available from corresponding author upon reasonable request.

Acknowledgments

This work has supported by the National Research Foundation of Korea (NRF) grant funded by the Korea government (MSIT) (No. 2021R1C1C1012119), the Chung-Ang University Graduate Research Scholarship in 2023, and the Korea Institute of Energy Technology Evaluation and Planning(KETEP) and the Ministry of Trade, Industry & Energy(MOTIE) of the Republic of Korea (No. 20214000000280).

Appendix A. Supplementary data

Supplementary data to this article can be found online at https://doi.org/10.1016/j.icheatmasstransfer.2024.107558.

References

[1] M. Meinshausen, N. Meinshausen, W. Hare, S.C.B. Raper, K. Frieler, R. Knutti, et al., Greenhouse-gas emission targets for limiting global warming to 2 °C, Nature 458 (2009) 1158–1162, https://doi.org/10.1038/nature08017.
[2] R. Hannappel, The Impact of Global Warming on the Automotive Industry, Bohol, Philippines, 2017, p. 060001, https://doi.org/10.1063/1.4996530.
[3] A. Stoppato, A. Benato, The importance of energy storage, Energy Storage (2017) 26.
[4] F. Liu, F. Zhao, Z. Liu, H. Hao, China's electric vehicle deployment: energy and greenhouse gas emission impacts, Energies 11 (2018) 3353, https://doi.org/10.3390/en11123353.
[5] J. Lin, X. Liu, S. Li, C. Zhang, S. Yang, A review on recent progress, challenges and perspective of battery thermal management system, Int. J. Heat Mass Transf. 167 (2021) 120834, https://doi.org/10.1016/j.ijheatmasstransfer.2020.120834.
[6] H. Liu, Z. Wei, W. He, J. Zhao, Thermal issues about Li-ion batteries and recent progress in battery thermal management systems: a review, Energy Convers. Manag. 150 (2017) 304–330, https://doi.org/10.1016/j.enconman.2017.08.016.
[7] R. Schmuch, R. Wagner, G. Hörpel, T. Placke, M. Winter, Performance and cost of materials for lithium-based rechargeable automotive batteries, Nat. Energy 3 (2018) 267–278, https://doi.org/10.1038/s41560-018-0107-2.
[8] M. S, R. M, R. S, Synthesis of surface modified LiFePO4 cathode material via polyol technique for high rate lithium secondary battery, Appl. Surf. Sci. 337 (2015) 234–240, https://doi.org/10.1016/j.apsusc.2015.02.100.
[9] J. Lee, P. Kumar, B.M. Moudgil, R.K. Singh, Electrochemical enhancement of LiFePO4 as a cathode material by incorporating Cu flakes for lithium ion rechargeable battery, Solid State Ionics 231 (2013) 18–24, https://doi.org/10.1016/j.ssi.2012.10.015.
[10] R. Marom, S.F. Amalraj, N. Leifer, D. Jacob, D. Aurbach, A review of advanced and practical lithium battery materials, J. Mater. Chem. 21 (2011) 9938, https://doi.org/10.1039/c0jm04225k.
[11] S. Pelletier, O. Jabali, G. Laporte, M. Veneroni, Battery degradation and behaviour for electric vehicles: review and numerical analyses of several models, Transp. Res. B Methodol. 103 (2017) 158–187, https://doi.org/10.1016/j.trb.2017.01.020.
[12] M.M. Hoque, M.A. Hannan, A. Mohamed, A. Ayob, Battery charge equalization controller in electric vehicle applications: a review, Renew. Sust. Energ. Rev. 75 (2017) 1363–1385, https://doi.org/10.1016/j.rser.2016.11.126.
[13] W. Wu, S. Wang, W. Wu, K. Chen, S. Hong, Y. Lai, A critical review of battery thermal performance and liquid based battery thermal management, Energy Convers. Manag. 182 (2019) 262–281, https://doi.org/10.1016/j.enconman.2018.12.051.
[14] X. Han, L. Lu, Y. Zheng, X. Feng, Z. Li, J. Li, et al., A review on the key issues of the lithium ion battery degradation among the whole life cycle, eTransportation 1 (2019) 100005, https://doi.org/10.1016/j.etran.2019.100005.
[15] J. Vetter, P. Novák, M.R. Wagner, C. Veit, K.-C. Möller, J.O. Besenhard, et al., Ageing mechanisms in lithium-ion batteries, J. Power Sources 147 (2005) 269–281, https://doi.org/10.1016/j.jpowsour.2005.01.006.
[16] J. Kim, E. Kwak, K. Oh, Degradation pathways dependency of a lithium iron phosphate battery on temperature and compressive force, Int. J. Energy Res. 45 (2021) 6888–6906, https://doi.org/10.1002/er.6280.
[17] M. Fleckenstein, O. Bohlen, M.A. Roscher, B. Bäker, Current density and state of charge inhomogeneities in Li-ion battery cells with LiFePO4 as cathode material due to temperature gradients, J. Power Sources 196 (2011) 4769–4778, https://doi.org/10.1016/j.jpowsour.2011.01.043.
[18] T. Grandjean, A. Barai, E. Hosseinzadeh, Y. Guo, A. McGordon, J. Marco, Large format lithium ion pouch cell full thermal characterisation for improved electric vehicle thermal management, J. Power Sources 359 (2017) 215–225, https://doi.org/10.1016/j.jpowsour.2017.05.016.
[19] T. Waldmann, G. Bisle, B.-I. Hogg, S. Stumpp, M.A. Danzer, M. Kasper, et al., Influence of cell design on temperatures and temperature gradients in lithium-ion cells: an In operando study, J. Electrochem. Soc. 162 (2015) A921–A927, https://doi.org/10.1149/2.0561506jes.
[20] J. Chen, D. Ren, H. Hsu, L. Wang, X. He, C. Zhang, et al., Investigating the thermal runaway features of lithium-ion batteries using a thermal resistance network model, Appl. Energy 295 (2021) 117038, https://doi.org/10.1016/j.apenergy.2021.117038.
[21] K. Chen, M. Song, W. Wei, S. Wang, Structure optimization of parallel air-cooled battery thermal management system with U-type flow for cooling efficiency improvement, Energy 145 (2018) 603–613, https://doi.org/10.1016/j.energy.2017.12.110.
[22] Q. Wang, P. Ping, X. Zhao, G. Chu, J. Sun, C. Chen, Thermal runaway caused fire and explosion of lithium ion battery, J. Power Sources 208 (2012) 210–224, https://doi.org/10.1016/j.jpowsour.2012.02.038.
[23] S. Abada, G. Marlair, A. Lecocq, M. Petit, V. Sauvant-Moynot, F. Huet, Safety focused modeling of lithium-ion batteries: a review, J. Power Sources 306 (2016) 178–192, https://doi.org/10.1016/j.jpowsour.2015.11.100.
[24] A.A. Pesaran, Battery thermal models for hybrid vehicle simulations, J. Power Sources 110 (2002) 377–382, https://doi.org/10.1016/S0378-7753(02)00200-8.
[25] J.-H. Seo, M.S. Patil, C.-P. Cho, M.-Y. Lee, Heat transfer characteristics of the integrated heating system for cabin and battery of an electric vehicle under cold weather conditions, Int. J. Heat Mass Transf. 117 (2018) 80–94, https://doi.org/10.1016/j.ijheatmasstransfer.2017.10.007.
[26] K. Chen, W. Wu, F. Yuan, L. Chen, S. Wang, Cooling efficiency improvement of air-cooled battery thermal management system through designing the flow pattern, Energy 167 (2019) 781–790, https://doi.org/10.1016/j.energy.2018.11.011.
[27] X.W. Lin, Z.F. Zhou, X.G. Zhu, B. Chen, H. Zhu, N.Y. Ben, X.D. Wang, W.W. Xu, Non-uniform thermal characteristics investigation of three-dimensional electrochemical-thermal coupled model for pouch lithium-ion battery, J. Clean. Prod. 417 (2023) 137912, https://doi.org/10.1016/j.jclepro.2023.137912.
[28] L. Liang, Y. Zhao, Y. Diao, R. Ren, H. Jing, Inclined U-shaped flat microheat pipe array configuration for cooling and heating lithium-ion battery modules in electric vehicles, Energy 235 (2021) 121433, https://doi.org/10.1016/j.energy.2021.121433.
[29] P.R. Tete, M.M. Gupta, S.S. Joshi, Developments in battery thermal management systems for electric vehicles: a technical review, J Energy Storage 35 (2021) 102255, https://doi.org/10.1016/j.est.2021.102255.
[30] X.W. Lin, Z.F. Zhou, T.F. Liu, S.Q. Xue, Y. Liang, L.F. Zhang, B. Liu, Rate capability and Ragone plots for designing battery thermal management system based on phase change material, J Energy Storage 74 (2023) 109539, https://doi.org/10.1016/j.est.2023.109539.
[31] O. Kalkan, A. Celen, K. Bakirci, Experimental and numerical investigation of the LiFePO4 battery cooling by natural convection, J Energy Storage 40 (2021) 102796, https://doi.org/10.1016/j.est.2021.102796.
[32] T. Wang, K.J. Tseng, J. Zhao, Z. Wei, Thermal investigation of lithium-ion battery module with different cell arrangement structures and forced air-cooling strategies, Appl. Energy 134 (2014) 229–238, https://doi.org/10.1016/j.apenergy.2014.08.013.
[33] K. Chen, Y. Chen, Y. She, M. Song, S. Wang, L. Chen, Construction of effective symmetrical air-cooled system for battery thermal management, Appl. Therm. Eng. 166 (2020) 114679, https://doi.org/10.1016/j.applthermaleng.2019.114679.
[34] N. Yang, X. Zhang, G. Li, D. Hua, Assessment of the forced air-cooling performance for cylindrical lithium-ion battery packs: a comparative analysis between aligned and staggered cell arrangements, Appl. Therm. Eng. 80 (2015) 55–65, https://doi.org/10.1016/j.applthermaleng.2015.01.049.
[35] J. Shen, Y. Wang, G. Yu, H. Li, Thermal management of prismatic lithium-ion battery with minichannel cold plate, J. Energy Eng. 146 (2020) 04019033, https://doi.org/10.1061/(ASCE)EY.1943-7897.0000621.
[36] C. Zhao, A.C.M. Sousa, F. Jiang, Minimization of thermal non-uniformity in lithium-ion battery pack cooled by channeled liquid flow, Int. J. Heat Mass Transf. 129 (2019) 660–670, https://doi.org/10.1016/j.ijheatmasstransfer.2018.10.017.
[37] X. Zhang, Z. Li, L. Luo, Y. Fan, Z. Du, A review on thermal management of lithium-ion batteries for electric vehicles, Energy 238 (2022) 121652, https://doi.org/10.1016/j.energy.2021.121652.
[38] T.E. Sarvey, Y. Zhang, L. Zheng, P. Thadesar, R. Gutala, C. Cheung, et al., Embedded cooling technologies for densely integrated electronic systems, in: 2015 IEEE Custom Integrated Circuits Conference (CICC), San Jose, CA, USA, IEEE, 2015, pp. 1–8, https://doi.org/10.1109/CICC.2015.7338365.
[39] D. Kong, Y. Kim, M. Kang, E. Song, Y. Hong, H.S. Kim, et al., A holistic approach to thermal-hydraulic design of 3D manifold microchannel heat sinks for energy-

efficient cooling, Case Stud. Therm. Eng. 28 (2021) 101583, https://doi.org/10.1016/j.csite.2021.101583.
[40] N. Wu, X. Ye, J. Yao, X. Zhang, X. Zhou, B. Yu, Efficient thermal management of the large-format pouch lithium-ion cell via the boiling-cooling system operated with intermittent flow, Int. J. Heat Mass Transf. 170 (2021) 121018, https://doi.org/10.1016/j.ijheatmasstransfer.2021.121018.
[41] H. Hirano, T. Tajima, T. Hasegawa, T. Sekiguchi, M. Uchino, Boiling liquid battery cooling for electric vehicle, in: 2014 IEEE Conference and Expo Transportation Electrification Asia-Pacific (ITEC Asia-Pacific), Beijing, China, IEEE, 2014, pp. 1–4, https://doi.org/10.1109/ITEC-AP.2014.6940931.
[42] X.W. Lin, Y.B. Li, W.T. Wu, Z.F. Zhou, B. Chen, Advances on two-phase heat transfer for lithium-ion battery thermal management, Renew. Sust. Energ. Rev. 189 (2024) 114052, https://doi.org/10.1016/j.rser.2023.114052.
[43] X.W. Lin, Z.F. Zhou, J. Yin, X.G. Zhu, M.Y. Shi, B. Chen, A comparative investigation of two-phase immersion thermal management system for lithium-ion battery pack, J. Clean. Prod. 434 (2024) 140472, https://doi.org/10.1016/j.jclepro.2023.140472.
[44] N.P. Williams, D. Trimble, S.M. O'Shaughnessy, Liquid immersion thermal management of lithium-ion batteries for electric vehicles: an experimental study, J Energy Storage 72 (2023) 108636, https://doi.org/10.1016/j.est.2023.108636.
[45] A. Kalani, S.G. Kandlikar, Enhanced pool boiling with ethanol at subatmospheric pressures for electronics cooling, J. Heat Transf. 135 (2013) 111002, https://doi.org/10.1115/1.4024595.
[46] H. Lee, T. Maitra, J. Palko, C. Zhang, M. Barako, Y. Won, et al., Copper inverse opal surfaces for enhanced boiling heat transfer, in: ASME 2017 International Technical Conference and Exhibition on Packaging and Integration of Electronic and Photonic Microsystems, American Society of Mechanical Engineers, San Francisco, California, USA, 2017, https://doi.org/10.1115/IPACK2017-74090 p. V001T01A006.
[47] Z. Yao, Y.-W. Lu, S.G. Kandlikar, Effects of nanowire height on pool boiling performance of water on silicon chips, Int. J. Therm. Sci. 50 (2011) 2084–2090, https://doi.org/10.1016/j.ijthermalsci.2011.06.009.
[48] C. Li, Z. Wang, P.-I. Wang, Y. Peles, N. Koratkar, G.P. Peterson, Nanostructured copper interfaces for enhanced boiling, Small 4 (2008) 1084–1088, https://doi.org/10.1002/smll.200700991.
[49] D. Kong, M. Kang, K.Y. Kim, J. Jang, J. Cho, J.B. In, et al., Hierarchically structured laser-induced graphene for enhanced boiling on flexible substrates, ACS Appl. Mater. Interfaces 12 (2020) 37784–37792, https://doi.org/10.1021/acsami.0c11402.
[50] J. Lin, Z. Peng, Y. Liu, F. Ruiz-Zepeda, R. Ye, E.L.G. Samuel, et al., Laser-induced porous graphene films from commercial polymers, Nat. Commun. 5 (2014) 5714, https://doi.org/10.1038/ncomms6714.
[51] M. Hou, Y. Bu, Y. Chen, Y. Guo, G. Wen, X. Chen, Fast-printed laser-induced-graphene pattern enabling directional thermal manipulation, Int. J. Heat Mass Transf. 197 (2022) 123303, https://doi.org/10.1016/j.ijheatmasstransfer.2022.123303.
[52] R.J. Moffat, Describing the Uncertainties in Experimental Results (n.d.), 2024, p. 15.
[53] A.C. Ferrari, J.C. Meyer, V. Scardaci, C. Casiraghi, M. Lazzeri, F. Mauri, et al., Raman spectrum of graphene and graphene layers, Phys. Rev. Lett. 97 (2006) 187401, https://doi.org/10.1103/PhysRevLett.97.187401.
[54] L.X. Duy, Z. Peng, Y. Li, J. Zhang, Y. Ji, J.M. Tour, Laser-induced graphene fibers, Carbon 126 (2018) 472–479, https://doi.org/10.1016/j.carbon.2017.10.036.
[55] L. Cao, S. Zhu, B. Pan, X. Dai, W. Zhao, Y. Liu, et al., Stable and durable laser-induced graphene patterns embedded in polymer substrates, Carbon 163 (2020) 85–94, https://doi.org/10.1016/j.carbon.2020.03.015.
[56] Z. Yang, C. Xu, H. Yan, Y. Liu, C. Yue, L. Zhang, et al., Laser-induced graphene assisting self-conversion reaction for sulfur-free aqueous Cu-S battery, Adv. Funct. Mater. 31 (2021) 2103893, https://doi.org/10.1002/adfm.202103893.
[57] B. Wu, Z. Li, J. Zhang, Thermal design for the pouch-type large-format lithium-ion batteries: I. Thermo-electrical modeling and origins of temperature non-uniformity, J. Electrochem. Soc. 162 (2015) A181–A191, https://doi.org/10.1149/2.0831501jes.
[58] L. Liu, J. Park, X. Lin, A.M. Sastry, W. Lu, A thermal-electrochemical model that gives spatial-dependent growth of solid electrolyte interphase in a Li-ion battery, J. Power Sources 268 (2014) 482–490, https://doi.org/10.1016/j.jpowsour.2014.06.050.
[59] Y.Y. Hsu, On the size range of active nucleation cavities on a heating surface, J. Heat Transf. 84 (1962) 207–213, https://doi.org/10.1115/1.3684339.